# Small-angle ($e^-$, Na) scattering in the 6—25-eV range

B. Jaduszliwer, P. Weiss,* A. Tino,* and B. Bederson
*Physics Department, New York University, New York, New York 10003*
(Received 26 March 1984)

We have investigated elastic and inelastic scattering of electrons by sodium atoms at intermediate energies (6—25 eV) by the atomic-recoil technique, using a new atomic-beams apparatus. The effects of the apparatus geometry, atomic velocity, and electron energy distributions on the analysis of the experimental results have been examined in detail, and their effects on small-angle scattering have been incorporated into the present work. We present absolute measurements of the elastic ($e^-$, Na) differential cross section at 10 eV for electron polar angles ranging between 12° and 22°. These measurements are in good agreement with the normalized results of S. K. Srivastava and L. Vuskovic [J. Phys. B 13, 2633 (1980)] and in reasonable agreement with the two-state close-coupling calculation of M. R. Issa (Ph.D. thesis, University of Durham, 1977). We also present absolute measurements of an integral over small angles of the $3\,^2P$ impact-excitation differential cross section, together with a precise prescription for comparison with theory. We found that the distorted-wave—polarized-orbital calculation of J. V. Kennedy, V. P. Myerscough, and M. R. C. McDowell [J. Phys. B 10, 3759 (1977)] gives results which are too high in the forward direction, while those of Issa are somewhat low.

## I. INTRODUCTION

Alkali-metal atoms are ideally suited for the production of atomic beams, can be easily detected, have large electron collision cross sections, are hydrogenic in their electron configuration, and the very strong coupling between the ground $n\,^2S$ and the $n\,^2P$ excited states in many cases simplifies the theoretical treatment of the collision problem. All these properties make them irresistable "targets of opportunity" for electron-atom collision research, be it experimental or theoretical.

Most of the experimental work has thus far been performed with ground-state Na and K atoms, and includes the measurement of total,[1–4] differential,[5–13] direct differential,[7] and exchange differential[14,15] elastic cross sections, as well as total[16,17] and differential[5,10,12,13,18–22] $n\,^2S$–$n\,^2P$ impact-excitation cross sections, with and without spin analysis. At low energies the unifying feature of these experiments is the generally good and sometimes excellent agreement existing between measurements and the results of few-state close-coupling calculations.[23–27] With regard to other theoretical approaches Sinfailam and Nesbet[28] calculated variational phase shifts below the first excitation threshold; their results for Na are in very good agreement with the close-coupling results of Moores and Norcross.[25] Another frequently used method is that of "polarized orbitals."[29] Burke[30] has shown that this method in its original form, where the polarization potential is determined using perturbation theory, gives an overly attractive potential for highly polarizable systems like the alkali-metal atoms. Stone[31] described a way to obtain the potential variationally, rather than by perturbation theory, and Lan[32] used Stone's method in an otherwise conventional polarized-orbitals calculation.

It is generally accepted that at high enough energies the first Born approximation describes quite accurately many collision processes, although there is no definitive prescription to specify the energy or angular range for which it can be used. In the intermediate energy range, defined loosely as the energy range in which a large number of scattering channels are open but the first Born approximation is not yet generally considered to be valid, a number of theoretical models have been developed to cope with a very complex problem. Bransden and McDowell[33] have reviewed both the general theoretical techniques used in this energy range, and the current experimental and theoretical situation for a number of atomic and ionic targets. For Na and K, two-state coupling calculations at intermediate energies have been performed by Carse,[34] Barnes *et al.*,[35] and Korff *et al.*;[36] the latter also did three-, seven-, and eight-state calculations to study the convergence of the method. None of these authors incorporated exchange. Issa[37] did two-state close-coupling calculations both with and without exchange. Walters[38] studied elastic scattering, as well as electron impact excitation of the first excited states, using the Glauber approximation, and Kennedy *et al.*[39] calculated electron impact-excitation differential cross sections using a unitarized distorted-wave—polarized-orbitals technique. The experimental results in this energy range are rather sparse, and there is an almost total lack of absolute measurements, that is to say, measurements which do not require normalization to theory at some energy or angle. The agreement between experiment and theory is only qualitative at best.

This paper reports on atomic-recoil studies of small-angle elastic and inelastic scattering of electrons by sodium atoms at intermediate energies, performed using a new atomic beams apparatus at New York University, which is described in detail in Sec. II. The atomic-recoil technique, in which post-collisional observations are made on

 

the recoiled atoms, rather than on the scattered electron, is discussed in Sec. III. Sections IV and V describe the elastic and inelastic scattering experiments, respectively, and present our results, which are absolute in the sense discussed above. Particular attention is paid to the effects of the finite angular resolution of the apparatus upon the measurements in each case.

## II. THE APPARATUS

The apparatus used for the experiments reported in this paper has been built to exploit the main advantages of the atomic-recoil technique, derived from the fact that the post-collisional observations are made on the atom, rather than on the electron: first, absolute cross sections can be measured without the need to determine the actual number density of atoms in the target beam, as will be discussed further in the next sections, and, second, by determining the atomic state before and after the collision, spin-exchange, or, more generally, angular-momentum-changing collisions can be investigated. Other design considerations were dictated by the desire to reduce as much as possible the "number" of initial and final states[40] over which the actual cross sections are averaged and summed to yield the smeared effective cross section which is the result of any real collision experiment, and also the sometimes conflicting goal of increasing the signal-to-noise ratio.

### A. General overview

A combination of long geometry, good collimation, and velocity selection of the atomic beam are necessary to have good angular resolution in atomic-recoil experiments. Figure 1 shows the general layout of the apparatus, which consists of four stainless-steel vacuum chambers and a long drift tube. The apparatus is mounted on a rigid aluminum structure which in turn is supported by four pneumatic vibration isolators. The first two chambers are pumped by diffusion pumps topped by water-cooled baffles, a 10-in. pump for the first (source) chamber and a 4-in. pump for the second (intermediate) chamber. The third (collision) chamber is pumped by a 300-liter/sec ion pump and the fourth (detector) chamber by a 150-liter/sec ion pump. A Ti sublimation pump adds some pumping capacity at the middle of the 300-cm-long drift tube interconnecting the last two chambers. The overall length of the vacuum envelope is 500 cm.

Each of the chambers can be moved on its mounting platform for coarse alignment of the apparatus. For finer alignment, all internal components are coupled to external precision positioners through vacuum bellows.

The detector chamber is mounted on the far end of an aluminum boom, the near end of which is attached to a rotary altazimuth[41] mount that in turn is rigidly attached to the collision chamber and centered on the collision volume. The drift tube is joined to the collision chamber by very flexible vacuum bellows, its other end is rigidly attached to the detector chamber, and its weight rests on the aluminum boom. In this fashion, the detector can move over the surface of a sphere of 335 cm radius centered at the collision volume, thus enabling us to perform two-dimensional scans of the angular distribution of atoms which have recoiled in collisions with electrons. The detector chamber is coupled through a precision universal joint to a two-dimensional positioner driven by stepping motors. The boom is suitably counterweighted, to present an essentially null load to the motors. An auxiliary HeNe laser can be mounted on the apparatus axis at the source end, for alignment purposes.

### B. The beam source

Crossed-beam scattering studies usually require lengthy periods of data taking, and consequently one of the main

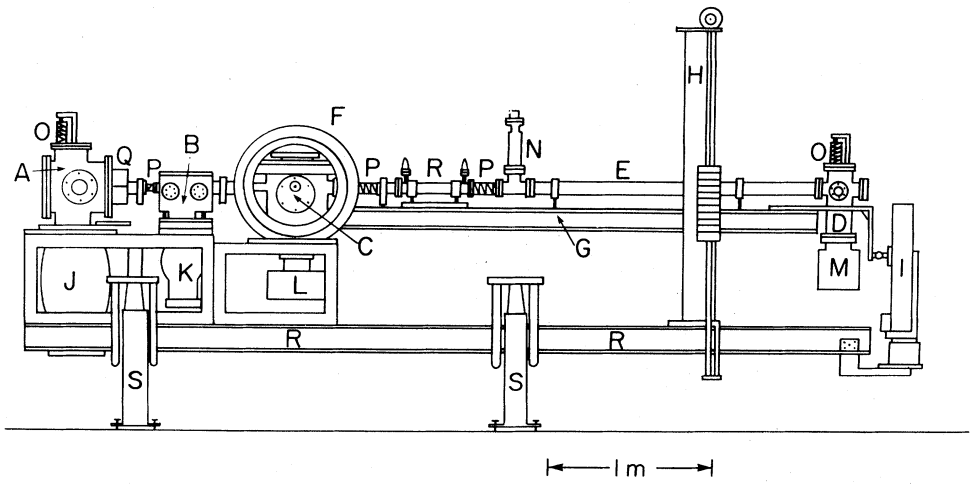


FIG. 1. General apparatus lay-out. *A*, source chamber; *B*, intermediate chamber; *C*, collision chamber; *D*, detector chamber; *E*, drift tube; *F*, altazimuth mount providing two-dimensional scanning motion for the detector; *G*, movable detector boom; *H*, counterweight system; *I*, detector positioner; *J*, 10-in. diffusion pump; *K*, 4-in. diffusion pump; *L*, 300-l/sec ion pump; *M*, 150-l/sec ion pump; *N*, Ti sublimation pump; *O*, internal component positioner; *P*, flexible bellows; *Q*, hexapole magnetic coils and yoke; *R*, aluminum mounting structure; *S*, vibration isolators.

considerations in designing the atomic-beam source was to insure reliable operation for extended periods of time. The need to operate it over a broad range of temperatures was another important consideration. Figure 2 shows a schematic drawing of the source and its surrounding oven. The source is a large horizontal cylindrical stainless-steel container, 220 $cm^3$ in volume, with a pipe-threaded hole on one of the ends, which acts as the loading port. After loading, a snout made of a standard stainless-steel capped pipe fitting closes the hole. As the edges of the fitting protrude into the container, molten material creep into the snout is minimized. The atomic beam effuses through a 0.04-cm orifice drilled in the cap. The source is large enough to supply several hundred hours of intense effusive beams of alkali-metal atoms or alkali-halide molecules.

The loaded source nests snugly inside a cylindrical stainless-steel oven heated by a MgO-insulated, stainless-steel-clad nichrome wire heater.[42] Within the oven, a smaller "superheater" of similar design surrounds the snout, so that it can be maintained hotter than the principal container during operation. In this way, the dimer fraction in the atomic beam can be reduced considerably; clogging of the exit orifice is also greatly reduced by this arrangement.

Two wells fitted with chromel-allumel thermocouples are provided, one for the main heater and one for the snout superheater. Independent proportional temperature controller circuits supply the power for the heaters, and the feedback loops have been carefully adjusted to avoid temperature overshoots or oscillations.

The oven fits inside a cylindrical triple heat shield, which in turn is surrounded by a water-cooled jacket. A removable cover and triple heat shield close the opening at the back end; at the front end there is a water-cooled plate with a 0.32-cm orifice for the atomic beam to pass through. To prevent large heat losses to that plate, it also carries a triple heat shield, with a 1-cm hole for the atomic beam. This geometry allows for most of the excess material effusing from the oven to condense on the cold plate, thus preventing the formation of a gas cloud in front of the oven orifice, which would broaden the beam and distort its shape. A heater allows us to periodically melt the material deposited on the plate, thereby avoiding clogging.

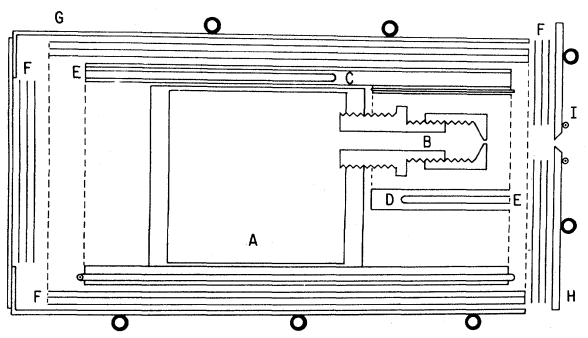


FIG. 2. Beam source and oven. *A*, source container; *B*, source snout; *C*, source heater; *D*, snout superheater; *E*, thermocouple well; *F*, triple heat shield; *G*, water-cooled jacket; *H*, water-cooled front plate; *I*, heater.

The source has been operating reliably for several thousand hours at temperatures between 200 °C and 800 °C; temperature differentials of up to 80 °C can be maintained routinely between the source and the snout.

Immediately after the cold plate the beam passes along the axis of a hexapole magnet, which in the experiments described here[43] serves the purpose of focusing[44] the beam at the detector, thus increasing the beam intensity, and also providing some velocity resolution, since the focal length of the device is velocity dependent.[45] In order to be able to optimize the focusing properties of the hexapole magnet for the several alkali-metal elements, a variable-current electromagnet was employed rather than a more conventional permanent magnet. The pole pieces, coil cores, and yoke were built of low-carbon steel;[46] the pole pieces are located inside the vacuum system, within a thin-walled stainless-steel tube which acts as the vacuum envelope. The coils and yoke are outside the vacuum, thus minimizing the problems of heat transfer and vacuum outgassing. The loss of flux in the gap at the vacuum envelope is insignificant. Each coil consists of 41 turns of 0.025-cm-thick, 4.45-cm-wide copper tape, insulated on one side with adhesive polyethylene tape. This configuration can be used with currents of up to 50 A without requiring any cooling.

The radius of the cylindrical space between the pole tips is 0.15 cm, and the length of the magnet is 14.5 cm; its experimentally determined focusing properties for sodium are very close to the calculated values.

A simple surface ionization detector, consisting of a hot 92% Pt, 8% W alloy wire and an ion collector, is located in the intermediate chamber. It normally monitors the edge of the atomic beam; it can be translated across the beam, and it is used mainly for malfunction diagnosis.

### C. The electron gun

The electron gun used in the present experiments is a modified version of one described previously.[47] It consists of a stack of planar components aligned by four accurately located ceramic rods. Figure 3 shows the stack sequence. A large molybdenum block is the foundation of the structure, providing support for the oxide-coated cathode and holes for the ceramic alignment rods. The cathode is of the type used in 4D32 vacuum tubes, and is supplied with a filament heater. It is grounded in normal gun operation. A heat shield made out of 0.005-cm-thick tantalum sheet prevents excessive heat loss from the cathode to the mounting block.

The electrodes are separated by aluminum-oxide spacers. Two thicknesses are used, 0.025 and 0.051 cm. The slits, grid, anode, and slitted anode are made out of 0.005-cm molybdenum sheet, and the blocks defining the equipotential channel where the collisions take place are also machined out of molybdenum, as are some metal spacers. The pressure plate that tops the stack and clamps the assembly tight is made out of stainless steel. The main modifications in the present design are, first, an axial magnetic field is no longer used to confine the elec-

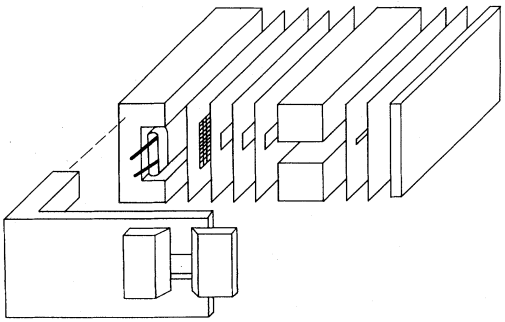

FIG. 3. Exploded view of the electron gun. Ceramic and metal spacers, ceramic alignment rods, fasteners, and the corresponding holes have been omitted for clarity. The sequence of components in the gun stack is, from left to right, support block, cathode, extracting grid, three-slit lens, top and bottom blocks defining the equipotential collision volume, slitted anode, anode, and pressure plate. The atomic-beam collimating slit is shown at the lower left-hand corner of the figure.

trons, and, second, all grids except the one nearest to the cathode have been replaced by slits to minimize secondary electron emission.

The slits used to define the electron beam at the overlap volume are 2.54 cm long and 0.08 cm high. The cross-sectional area of the electron beam in the collision region is then about 0.2 $cm^2$, allowing for fairly high electron currents without excessive electron current densities, which could seriously distort the shape of the equipotential surfaces at the collision region. On the other hand, since we are sampling a relatively large area of the cathode, great care has to be taken to insure the uniformity of the cathode surface; otherwise, a very broad electron energy distribution results.

The voltages applied at the different electrodes are chosen so as to avoid strong focusing, thus making the electron trajectories almost perpendicular to the planar electrodes. This can be checked by monitoring the current collected on the blocks defining the equipotential region, and minimizing it relative to the current collected at the anode.

The electron energy distribution can be measured using a retarding field technique, followed by numerical differentiation of the collected current versus retarding potential data. In order to reduce the effects of space charge in front of the retarding electrode, the measurement is performed on a small fraction of the electrons reaching the collector. This is achieved by applying a low accelerating potential to the slitted anode, and performing the retarding potential measurement at the anode, on the electrons passing through the narrow slit. When taking scattering data, both anodes are connected together.

The anode voltage is normally set at 60 V to reduce to a negligible level the number of secondary electrons emitted back into the collision volume. The observation of back-recoiled atoms is the most sensitive test of the presence of such secondaries. The narrowness of the equipotential channel makes field penetration from the anode at the beam overlap volume negligible.

The electron energy in the collision region is corrected for space charge and contact potential difference in the manner described by Collins.[48] The width of the electron energy distribution is about 0.5 eV, full width at half maximum (FWHM). This spread is considered adequate for the present study, which is concerned primarily with potential scattering.

A collimating slit, 0.118 cm high and 0.115 cm wide, mounted on the gun support block 1 cm upstream from the entrance to the collision channel defines the atomic beam at the overlap volume. A large double-walled high permeability shield keeps the magnetic field in the volume occupied by the electron gun well below $10^{-2}$ G.

A Digital Equipment Corporation PDP 11/03 computer which controls the experiment can turn the electron beam on or off by switching the first slit between the normal, positive operating voltage and a $-75$-V cutoff supply. The switch is actuated from the PDP 11/03 analog output port.

### D. The atomic detector

In the present experiment the sodium atoms are ionized on the surface of a 0.13-cm-wide, 0.038-cm-thick platinum ribbon (the "hot wire"), heated to 1000 °C. The detector time constant (the ion boil-off time) at that temperature is of the order of a few msec. A suitable mask defines an active detector area of $0.1\times0.1$ $cm^2$.

An einzel lens and an arrangement of four steering plates focus the sodium ions into the entrance orifice of a 90° sector magnetic, mass analyzer. A uniform transverse 6-kG magnetic field is provided by two SmCo permanent magnets, $2.5\times2.5\times0.64$ $cm^3$, mounted on a #404-stainless-steel yoke, leaving a 0.4-cm gap between pole-pieces. The detector is tuned for transmission of the desired mass number by adjusting the hot wire voltage.

The estimated ionization efficiency of the hot platinum wire is 0.95, and the overall transmission of the ion optics and mass analyzer was measured to be $\tau\simeq0.71$. The mass resolution of the analyzer was measured to be 0.27, against a design value of 0.25; the difference is attributable to lack of homogeneity in the magnetic field.

A high-current Channeltron electron multiplier is mounted with its input cone near the exit orifice of the mass analyzer, and the cone is biased at a high negative voltage. A guard electrode between analyzer and Channeltron prevents secondary electrons from being attracted out of the input cone.

The Channeltron can be operated at high gain, as a single particle detector, or a low gain, as an analog current amplifier. The single-particle counter mode can be used only when the count rates are relatively low, i.e., with the detector displaced from the beam axis. Near the beam axis analog operation is required, and care has to be exercised to keep the gain low enough to insure linearity. In the particle-counting mode, the Channeltron output pulses are preamplified at the detector chamber, and then, after passing through a shaping amplifier and single channel analyzer operated in the integral mode, are counted by a scaler. The scaler, in turn, is operated and read through the parallel digital port of the PDP 11/03 computer controlling the experiment. In the analog mode, the Chan-

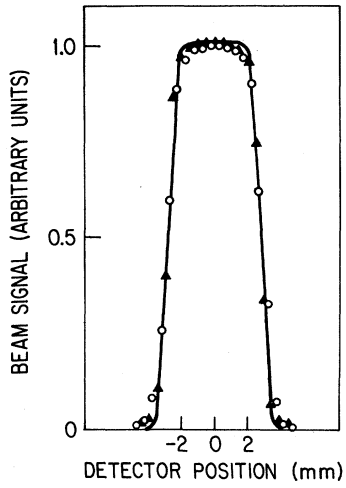


FIG. 4. Atomic-beam intensity profiles (hexapole magnet off). Solid line, calculated profiles; triangles, measured vertical profile; circles, measured horizontal profile.

neltron output current is fed through the required preamplifiers either to a high-sensitivity electrometer or to a lock-in amplifier. The output of either instrument is sampled by the analog-to-digital converter (ADC) of the PDP 11/03.

### E. The atomic beam

The atomic sodium beam is produced by heating high-purity sodium in the source container to about 400°C. With the hexapole magnet off, the velocity distribution in the resulting atomic current is the modified ($V^3$) Maxwellian; the most probable velocity is about 850 m/s. The unfocused beam number density at the collision region is approximately $3.5\times10^7$ cm$^{-3}$. Operating the source snout about 50°C hotter than the container insures that the dimer fraction in the atomic beam is smaller than $10^{-2}$. On the beam axis, the 0.01-cm$^2$ detector intercepts about $2\times10^9$ atoms per second.

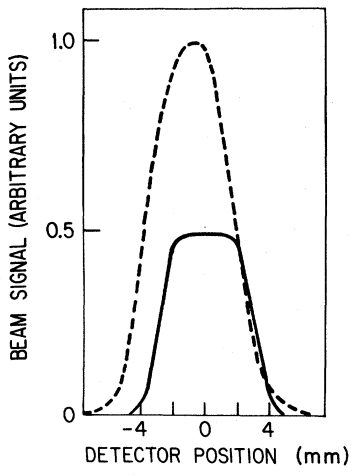


FIG. 5. Atomic-beam horizontal intensity profile. Solid line, hexapole magnet off; dashed line, hexapole magnet on. The small offset between both profiles is due to a small initial misalignment of the beam with respect to the axis of the hexapole magnet, which of course was irrelevant before energizing the magnet.

The intensity profile of the unfocused beam can be calculated using purely geometric[49] methods. Figure 4 shows the calculated profile, as well as the results of actual intensity measurements, displacing the detector across the beam both horizontally and vertically. As can be seen, the agreement is excellent.[50] The angular width of the beam is $1.4\times10^{-3}$ rad (FWHM).

Figure 5 shows the beam profile with the hexapole operating, with magnet current adjusted to give maximum beam intensity. Using the technique described in Sec. V, the average atomic speed in the focused beam was measured to be about 1000 m/s, and an upper bound for the width of the velocity distribution was obtained to be $\Delta V/V<0.25$ (FWHM).

## III. THE ATOMIC-RECOIL METHOD

We present here an (almost) complete kinematic analysis of the recoil-scattered beam problem. In a sense, despite the "crossed-beam" nature of the problem, one is dealing here with a situation which is closely related to the full solution of the Boltzmann collision integral, taken over the appropriate regions of configuration and momentum spaces.[51] Such an analysis is, in principle, always required in a crossed-beam experiment, except in the limiting, trivial case where details of the crossed-beam overlap integrals are ignored (as, by necessity, they often are). In the present case, where we are particularly interested in small-angle scattering, as well as for applications to electron scattering by highly polar molecules,[52] where small-angle scattering is dominant, the analysis is of particular relevance. The added complexity which results from the need to relate atom and electron scattering angles is balanced, we believe, by the resulting ability to study small-angle scattering without the need to be concerned with high-resolution electron optics in detection.

Figure 6 shows the atomic beam incident along the $y$ axis (momentum $M\vec{V}$) and the electron beam (momentum $m\vec{v}$) along the $z$ axis. After the collision the atomic and electron momenta are $M\vec{V}'$ and $m\vec{v}'$. Defining $\alpha=mv/MV$ and $\beta=mv'/MV$, the atomic-recoil angles $\psi$ (in the plane of the beams) and $\chi$ (in the normal plane containing $M\vec{V}'$) can be obtained in terms of the electron polar and azimuthal scattering angles $\theta$ and $\phi$ using energy and momentum conservation considerations. If the atom is initially in the ground state, and after the collision is left in a state labeled by $k$, then, to first order in $\alpha$ and $\beta$,

$$\psi=\alpha-\beta_k\cos\theta\ , \tag{1}$$

$$\chi=\beta_k\sin\theta\sin\phi\ , \tag{2}$$

and $V'=V$. In the present experiments, the largest value of $\alpha$ is 0.07, making the second-order corrections negligible. For elastic scattering, $\beta_k=\alpha$. Since in the present paper we will refer only to elastic scattering or impact excitation of the $3^2P$ state, excluding all other collision

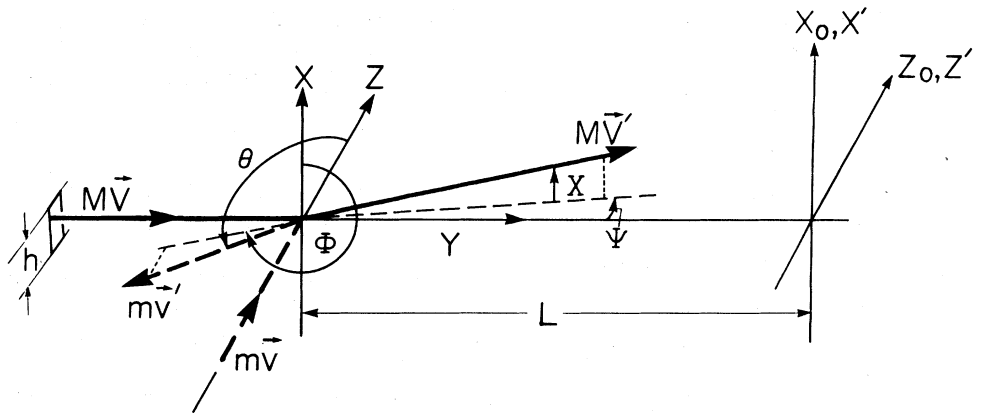


FIG. 6. Atomic-recoil and electron scattering angles. $M\vec{V},M\vec{V}'$, atomic momenta before and after the collision; $m\vec{v},m\vec{v}'$, electron momenta before and after the collision. $h$ is the height of the interaction volume, $L$ the distance between interaction volume and detector plane. In the absence of collisions an atom crosses the detector plane at $x_0,z_0$; after a collision, the coordinates are $x',z'$.

channels, in what follows we will forego the use of the subscript $k$.

In Eqs. (1) and (2) $\theta,\phi$ are the laboratory-frame electron scattering angles. The difference between laboratory-frame angles and center-of-mass-frame angles is negligible except for very small polar angles ($\theta\simeq 0.05°$) or energies very close to threshold ($E=1.001E^*$, where $E^*$ is the excitation energy of the $3^2P$ state, $E^*=2.10$ eV).

Let $x,y,z$ be the coordinates of an unscattered atom in the collision region, and $x_0,z_0$ its coordinates in the detector plane. The coordinates of a scattered atom in the detector plane are $x',z'$. The direction of motion of an unscattered atom is given by $\psi_0,\chi_0$ (both very small), while $\psi',\chi'$ (also small) specify that of the scattered atom. $\psi=\psi'-\psi_0$ and $\chi=\chi'-\chi_0$ are given by Eqs. (1) and (2).

The differential electron number current density within the collision region for electrons whose energies are in the range $dE$ is given by $\vec{j}(x,y,z;E)dE$. In the present analysis we do not include the effects of nonparallelism of the electron momenta. We will accordingly use $j$ to denote $j_z$, and assume $j_x=j_y=0$. The number density of atoms in this region with velocities lying within the angular range $d\psi_0,d\chi_0$, and possessing speeds in the range $dV$, is $n(x,y,z;\psi_0,\chi_0,V)d\psi_0 d\chi_0 dV$. We assume all atoms to be initially in the ground state.

The number of atoms in the volume $dx\,dy\,dz$ which will be left in the state labeled $i$ and recoiled into the angular range $d\psi',d\chi'$ after colliding with an electron of energy $E$ is, per unit time,

$$\begin{aligned} dN=&[j(x,y,z;E)dE\,dx\,dy] \\ &\times[n(x,y,z;\psi_0,\chi_0,V)d\psi_0 d\chi_0 dV] \\ &\times[\sigma_i'(\psi'-\psi_0,\chi'-\chi_0;E,V)d\psi'\,d\chi']dz\ , \end{aligned} \tag{3}$$

where $\sigma_i'(\psi'-\psi_0,\chi'-\chi_0;E,V)d\psi\,d\chi$ is the cross section for scattering an atom of velocity $V$ by an electron of energy $E$ into the angular range $d\psi\,d\chi$, after being left in the $i$th state by the collision. For the purposes of the present paper, $i=0$ implies elastic scattering, and $i=1$, impact excitation of the $3^2P$ state.

Since all the recoil angles are small, $\psi_0=(z_0-z)/(L-y)$, $\chi_0=(x_0-x)/(L-y)$, $d\psi_0=dz_0/(L-y)$, $d\chi_0=dx_0/(L-y)$, $\psi=\psi'-\psi_0=(z'-z_0)/(L-y)$, $\chi=\chi'-\chi_0=(x'-x_0)/(L-y)$, $d\psi'=dz'/(L-y)$, and $d\chi'=dx'/(L-y)$, where $L$ is the distance between the interaction region and the detector plane.

Let $\Delta N$ be the number of recoiled atoms reaching the detector per unit time after being left in the $i$th state in a collision with an electron of energy $E$. Then,

$$\begin{aligned} \Delta N=&\int j(x,y,z;E)\,n\left[x,y,z;\frac{z_0-z}{L-y},\frac{x_0-x}{L-y},V\right] \\ &\times\sigma_i'\left[\frac{z'-z_0}{L-y},\frac{x'-x_0}{L-y};E,V\right] \\ &\times dE\,dV\,dx\,dy\,dz\frac{dx'\,dz'}{(L-y)^2}\frac{dx_0\,dz_0}{(L-y)^2}\ . \end{aligned} \tag{4}$$

The number of unscattered atoms reaching $dx_0dz_0$ per second with speeds in the range of $dV$ per unit of time is

$$\begin{aligned} &J(x_0,z_0;V)dx_0dz_0dV \\ &\quad=V\,dV\,dx_0dz_0 \\ &\qquad\times\int n\left[x,y,z;\frac{z_0-z}{L-y},\frac{x_0-x}{L-y},V\right]\frac{dx\,dz}{(L-y)^2}\ . \end{aligned} \tag{5}$$

Since we assume $j(x,y,z;E)$ does not depend on $x,z$, we can integrate (5) over $dx\,dz$, obtaining

$$\begin{aligned} \Delta N=&\int j(y;E)\frac{J(x_0,z_0;V)}{V}\sigma_i'\left[\frac{z'-z_0}{L-y},\frac{x'-x_0}{L-y};E,V\right] \\ &\times dE\,dV\,dy\,dx_0dz_0\frac{dx'dz'}{(L-y)^2}\ . \end{aligned} \tag{6}$$

The number of electrons intersecting the atomic beam with energies in the range $dE$ per unit time is given by

$$i(E)dE = dE \int j(y;E)dx\,dy = h\,dE \int j(y;E)dy \ , \tag{7}$$

where $h$ is the height of the collision region, as shown in Fig. 6.

Since $L = 355$ cm and $0 < y < 2.5$ cm, $L - y \simeq L$, and then

$$\Delta N = \frac{1}{hL^2} \int i(E) J(x_0,z_0;V) \sigma_i' \left[ \frac{z'-z_0}{L}, \frac{x'-x_0}{L}; E, V \right] \times dE \frac{dV}{V} dx_0 dz_0 dx' dz' \ . \tag{8}$$

$\sigma_i'(\psi,\chi;E,V)$ depends on the electron energy in two ways: through its explicit energy dependency, and through the kinematic transformations relating $\psi$ and $\chi$ to $\theta$ and $\phi$. We have

$$\frac{1}{\alpha}\frac{\partial \alpha}{\partial E} = \frac{1}{2E} \quad \text{and} \quad \frac{1}{\beta}\frac{\partial \beta}{\partial E} = \frac{1}{2(E-E^*)} \tag{9}$$

so that if the kinetic energy of the electron after the collision ($E$ for elastic collisions, $E - E^*$ for inelastic collisions) is much larger than $\Delta E/4$, where $\Delta E$ is the width of the electron energy distribution (FWHM), then the implicit dependence of $\sigma_i'(\psi,\chi;E,V)$ on $E$ through the recoil angles can be neglected. This is indeed the case for the energy range which we have investigated in the present experiments, since $\Delta E \simeq 0.50$ eV. Thus, if we assume the cross section to be a slowly varying function of energy over the energy distribution, we can integrate over electron energies to get

$$\Delta N = \frac{I_e J_0}{hL^2} \int \mathscr{V}(V) \mathscr{f}(x_0) \mathscr{g}(z_0) \times \sigma_i' \left[ \frac{z'-z_0}{L}, \frac{x'-x_0}{L}; E_0, V \right] \times \frac{dV}{V} dx_0 dz_0 dx', dz' \ , \tag{10}$$

where $I_e$ is the total electron number current through the interaction region, $I_e = \int i(E)dE$, and $E_0$ is the nominal (peak) electron energy. In Eq. (10) we have also assumed that the atomic number current density at the detector plane, $J(x_0,z_0;V)$, can be factored as

$$J(x_0,z_0;V) = J_0 \mathscr{f}(x_0) \mathscr{g}(z_0) \mathscr{V}(V) \ , \tag{11}$$

where $\mathscr{f}$ and $\mathscr{g}$, the vertical and horizontal beam density profiles, are normalized to unit value at the origin (beam axis), while $\mathscr{V}(V)$, the velocity distribution function, is normalized to unit area. $J_0$ is then the velocity-integrated number current density on the beam axis. We have tested the geometric separability in Eq. (11), and it is satisfied quite accurately, as shown in Fig. 7. We are quite certain that the velocity distribution is also separable, although we have not been able to test that assumption. Using $x' = x_0 + \chi L$, $z' = z_0 + \psi L$ to change variables,

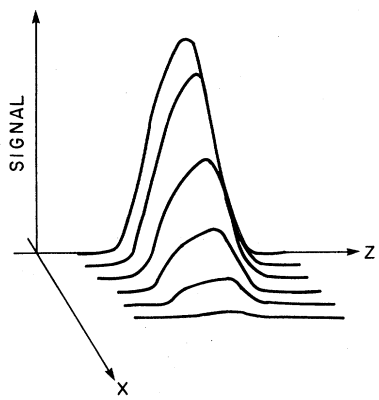


FIG. 7. Two-dimensional atomic-beam intensity profiles (hexapole magnet on).

$$\Delta N = \frac{I_e J_0}{h} \int \mathscr{V}(V) \mathscr{f}(x_0) \mathscr{g}(z_0) \times \sigma_i'(\psi,\chi;E_0,V) \frac{dV}{V} dx_0 dz_0 d\psi\, d\chi \ . \tag{12}$$

As shown in Fig. 8, the detector is a square of side $d$, centered at $x' = 0$, $z' = z_D$. Atoms with speed $V$ being recoiled into the detector by angles $\psi,\chi$ will come from a square of side $d$, centered at $x_0 = -\chi L$, $z_0 = z_D - \psi L$. Integration over $dx_0, dz_0$ then yields

$$\Delta N = \frac{I_e I_0}{h} \int \mathscr{V}(V) \mathscr{F}(-\chi L) \mathscr{G}(z_D - \psi L) \times \sigma_i'(\psi,\chi;E_0,V) \frac{dV}{V} d\psi\, d\chi \ , \tag{13}$$

where $\mathscr{F}(x_0), \mathscr{G}(z_0)$ are the measured beam profiles (i.e., the beam density profiles integrated over the detector area) and $I_0$ is the beam current at the origin, integrated over the velocity distribution and the detector area. $\mathscr{F}$ and $\mathscr{G}$ are also normalized to unity at the origin.

The beam boundaries, as shown in Fig. 3, are given by $X_1$, $X_2$, $Z_1$, and $Z_2$. Since

$$\sigma_i'(\psi,\chi;E_0,V) d\psi\, d\chi = \sigma_i(E_0,\theta) \sin\theta\, d\theta\, d\phi \tag{14}$$

we can write

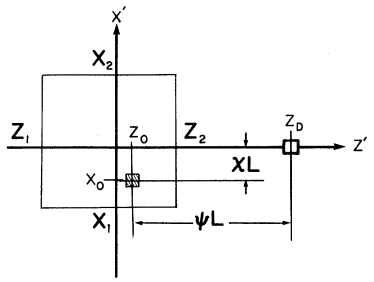


FIG. 8. Map of detector plane in the neighborhood of the atomic beam. Square detector (side $d$) is at $x' = 0$, $z' = z_D$. Atoms reaching the detector after being recoiled by $\psi,\chi$, in the absence of collisions would have crossed the detector plane at $x_0 = -\chi L$, $z_0 = z_D - \psi L$. $X_1$, $X_2$, $Z_1$, and $Z_2$ give the beam boundaries.

$$\Delta N=\frac{2I_eI_0}{h}\int\frac{dV}{V}\mathscr{V}(V)\int_{\Theta_1}^{\Theta_2}d\theta\sin\theta\,\sigma_i(E_0,\theta)\mathscr{G}(z_D-\alpha L-\beta L\cos\theta)\int_{\Phi_1}^{\Phi_2}\mathscr{F}(-\beta L\sin\theta\sin\phi)d\phi\ , \tag{15}$$

where the limits of integration are given by

$$\Phi_1=\arcsin(X_2/\beta L\sin\theta)\ \text{ if } X_2<\beta L\sin\theta;\ \ \Phi_1=-\pi/2\ \text{ if } X_2\geq\beta L\sin\theta \tag{16a}$$

$$\Phi_2=\arcsin(X_1/\beta L\sin\theta)\ \text{ if } -X_1<\beta L\sin\theta;\ \ \Phi_2=\pi/2\ \text{ if } -X_1\geq\beta L\sin\theta \tag{16b}$$

$$\Theta_1=\arccos[\alpha/\beta-(z_D-Z_2)/\beta L]\ \text{ if } z_D>Z_2;\ \ \Theta_1=0\ \text{ if } z_D\leq Z_2 \tag{17a}$$

$$\Theta_2=\arccos[\alpha/\beta-(z_D-Z_1)/\beta L]\ . \tag{17b}$$

The factor 2 arises because there are two values of $\phi$ yielding the same value of $\chi$, as shown by Eq. (2).

We define the "azimuthal form factor" $\gamma(\theta,V,E_0)$ as the fraction of azimuthal scattering angles leading to detectable recoil angles:

$$\gamma(\theta,V,E_0)=\frac{1}{\pi}\int_{\Phi_1}^{\Phi_2}\mathscr{F}(-\beta L\sin\theta\sin\phi)d\phi\ . \tag{18}$$

$\gamma(\theta,V,E_0)$ peaks strongly in the forward direction, as can easily be seen by inspecting the azimuthal integration limits, Eqs. (16). Figure 9 illustrates an example.

The number of atoms recoiled into the detector can be written as

$$\Delta N=2\pi\frac{I_eI_0}{h}\int\frac{dV}{V}\mathscr{V}(V)\times\int_{\Theta_1}^{\Theta_2}\sigma_i(E_0,\theta)\mathscr{G}(z_D-\alpha L-\beta L\cos\theta)\times\gamma(\theta,V,E_0)\sin\theta\,d\theta\ . \tag{19}$$

As $\gamma(\theta,V,E_0)$ peaks sharply in the forward direction, if $|z_d-(\alpha-\beta)L|<\Delta Z/2$, where $\Delta Z$ is the FWHM of the horizontal beam profile, forward scattering will provide the dominant contribution to $\Delta N$.

## IV. SMALL-ANGLE ELASTIC SCATTERING

Figure 10 shows schematically the experimental arrangement used for the present work. Combining Eqs. (1) and (2) for $\alpha=\beta$ shows that all atoms recoiled by elastic collisions will cross the detector plane within a circle of center $x'=0$, $z'=\alpha L$, and radius $R_0=\alpha L$. On the other hand, atoms recoiled after $3^2P$ state impact excitation will cross the detector within a circle of the same center, but a smaller radius, $R_1=\beta L$. Since only elastically recoiled atoms will be detected between $z'=0$ and $z'=(\alpha-\beta)L$, measurements of $\Delta N$ in that interval will in principle yield the elastic scattering differential cross section for polar angles ranging between $\theta=0$ and $\theta=\arccos(\beta/\alpha)=\arccos[(1-E^*/E)^{1/2}]$. In practice, the finite width of the atomic beam restricts this range quite severely. We have performed such measurement at $E=10$ eV, for $12.1°\leq\theta\leq21.8°$, where $\theta$ is the nominal polar scattering angle, determined by

$$\theta=\arccos(1-z_D/\alpha L)\ . \tag{20}$$

When the detector is at $x'=0$, $z'=z_D$ the atomic-beam signal at the detector is given by

$$S(z_D)=\epsilon I_0\mathscr{F}(0)\mathscr{G}(z_D)=\epsilon I_0\mathscr{G}(z_D)\ , \tag{21}$$

where $\epsilon$ is the overall efficiency of the detector system. The net scattering signal is

$$\Delta S(z_D)=\Delta S_{\text{in}}-\Delta S_{\text{out}}=\epsilon(\Delta N_{\text{in}}-\Delta N_{\text{out}})\ . \tag{22}$$

Defining an apparatus form factor

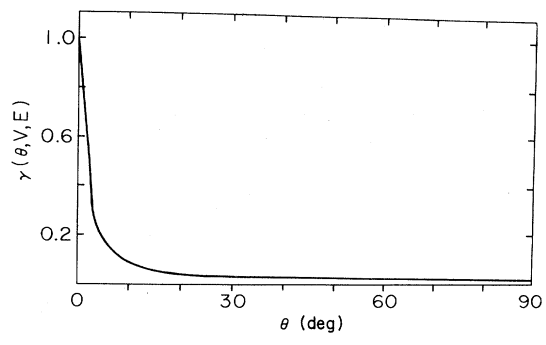


FIG. 9. Azimuthal form factor vs $\theta$, calculated for an electron energy $E_0=6$ eV and an atomic velocity of $V=\bar{V}=1000$ m/sec. For $\theta>90°$, $\gamma(\theta,V,E_0)=\gamma(180°-\theta,V,E_0)$.

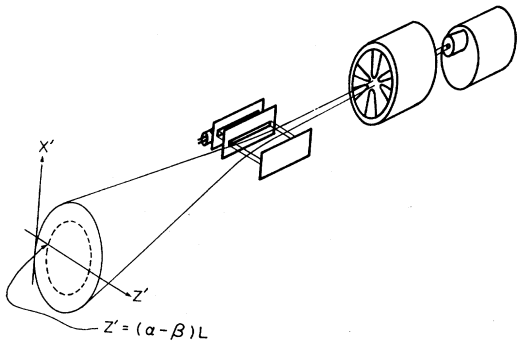


FIG. 10. Experimental arrangement. After focusing and velocity selection by the hexapole magnet, the atomic beam is crossfired by the electron beam. Atoms recoiled elastically will cross the detector plane within the solid circle (center at $x'=0$, $z'=\alpha L$, radius $\alpha L$). Atoms recoiled inelastically will cross the detector plane within the dashed circle [same center as above, radius $(\alpha-\beta)L$]. Elastic cross-section measurements can be performed between $z'=0$ and $z'=(\alpha-\beta)L$; forward inelastic scattering is detected at $z'=(\alpha-\beta)L$.

$$\Upsilon(\theta,\phi)=\mathscr{F}(-\alpha L\sin\theta\sin\phi)\mathscr{G}[z_D-\alpha L(1-\cos\theta)] \tag{23}$$

it follows that Eq. (19) can be rewritten, obtaining for the scattering-in contribution

$$\Delta N_{\text{in}}=2\frac{I_eI_0}{h}\int\frac{dV}{V}\mathscr{V}(V)\int\sigma_0(E_0,\theta)\Upsilon(\theta,\phi)d\Omega\ , \tag{24}$$

where

$$2\int\sigma_0(E_0,\theta)\Upsilon(\theta,\phi)d\Omega$$
$$=2\pi\int_{\Theta_1}^{\Theta_2}\sigma_0(E_0,\theta)\mathscr{G}[z_D-\alpha L(1-\cos\theta)]$$
$$\times\gamma(\theta,V,E_0)\sin\theta\,d\theta\ . \tag{25}$$

The scattering-out contribution $\Delta N_{\text{out}}$ is given by[3]

$$\Delta N_{\text{out}}=\frac{I_0I_e}{h}\left\langle\frac{1}{V}\right\rangle Q(E_0)\mathscr{G}(z_D)\ , \tag{26}$$

where $Q(E_0)$ is the total scattering cross section, and

$$\left\langle\frac{1}{V}\right\rangle=\bar{V}^{-1}=\int\frac{\mathscr{V}(V)}{V}dV\ . \tag{27}$$

The net scattering signal—to—atomic-beam signal ratio with the detector set at $x'=0$, $z'=z_D$, is

$$\frac{\Delta S(z_D)}{S(z_D)}=\frac{I_e}{h}\left[\frac{2}{\mathscr{G}(z_D)}\right.$$
$$\times\int\frac{dV}{v}\mathscr{V}(V)\int\sigma_0(E_0,\theta)\Upsilon(\theta,\phi)d\Omega$$
$$\left.-\left\langle\frac{1}{V}\right\rangle Q(E_0)\right]\ . \tag{28}$$

The integrals in Eq. (25) depend on the atomic speed $V$ through the arguments of the functions $\mathscr{F}$ and $\mathscr{G}$, and through the limits of integration, $\Theta_1$, $\Theta_2$, $\Phi_1$, and $\Phi_2$. It is easy to show that, for the range of angles explored in this experiment, $\delta\Theta/\Theta\simeq\frac{1}{2}\delta V/V$, and $\delta\Phi/\Phi\simeq\delta V/V$, where $\delta V/V\leq 0.125$, as discussed in Sec. V. If the velocity distribution is not too asymmetrical, and there are no extremely sharp features in the differential cross section, then the overall velocity dependence of those integrals is weak and smooth enough so that integration over the velocity distribution can be performed separately, yielding

$$\frac{\Delta S(z_D)}{S(z_D)}=\frac{I_e}{h}\left\langle\frac{1}{V}\right\rangle\left[\frac{2}{\mathscr{G}(z_D)}\int\sigma_0(E_0,\theta)\Upsilon(\theta,\phi)d\Omega\right.$$
$$\left.-Q(E_0)\right]\ . \tag{29}$$

The above assumptions were tested by numerical integration using several different model velocity distributions.

Manipulation of Eq. (29) finally gives

$$\int_{\Theta_1}^{\Theta_2}d\theta\sin\theta\,\sigma_0(E_0,\theta)\int_{\Phi_1}^{\Phi_2}\Upsilon(\theta,\phi)d\phi$$
$$=\Delta\sigma_0=\frac{\mathscr{G}(z_D)}{2}\left[Q(E_0)+\frac{h\bar{V}}{I_e}\frac{\Delta S(z_D)}{S(z_D)}\right] \tag{30}$$

allowing an absolute measurement of an integral of the elastic differential cross section. The electron number current through the interaction region has to be determined absolutely, but that does not present any special difficulty. In Eq. (30), $\Upsilon(\theta,\phi)$ is evaluated using $V=\bar{V}$. For the total scattering cross section at 10 eV we use the value measured by Kasdan *et al.*,[3] $Q(E_0)=(75\pm2.6)\times10^{-16}$ cm$^2$. $\bar{V}$ was determined daily as described in Sec. V and was quite consistent from day to day. The horizontal and vertical beam profiles were measured frequently, and also found to vary very little from day to day. Table I gives some values for these profiles; for intermediate points, linear interpolation is quite satisfactory.

$\Delta S(z_D)$ and $S(z_D)$ were measured with the Channeltron operating in the analog mode, its output current being fed into a high-sensitivity electrometer. The electron gun was alternately turned on and off, and in each case the electrometer voltage was sampled repeatedly by the computer ADC, as described in Sec. II. After many cycles the average detector signals with the electron gun on and off, $S_{\text{on}}$ and $S_{\text{off}}$, were calculated. Then

$$\frac{\Delta S(z_D)}{S(z_D)}=\frac{S_{\text{on}}-S_{\text{off}}}{S_{\text{off}}}\ . \tag{31}$$

This procedure was repeated many times cycling the detector through positions corresponding to $\Theta=12.1°$, 14.5°, 17.0°, 19.4°, and 21.8°, and $\mathscr{G}(z_D)$ was measured accurately each time. The right-hand-side formula in Eq.

TABLE I. Horizontal and vertical atomic beam profiles, normalized to unity at the beam axis.

| Detector displacement $x_0,z_0$ (cm) | Vertical profile $\mathscr{F}(x_0)$ | Horizontal profile $\mathscr{G}(z_0)$ |
|---|---|---|
| −0.61 | | 0 |
| −0.56 | | 0.025 |
| −0.51 | | 0.058 |
| −0.46 | | 0.103 |
| −0.41 | 0 | 0.149 |
| −0.36 | 0.057 | 0.200 |
| −0.31 | 0.177 | 0.267 |
| −0.25 | 0.359 | 0.412 |
| −0.20 | 0.559 | 0.632 |
| −0.15 | 0.719 | 0.809 |
| −0.10 | 0.835 | 0.916 |
| −0.05 | 0.933 | 0.980 |
| 0 | 1.000 | 1.000 |
| 0.05 | 0.992 | 0.978 |
| 0.10 | 0.895 | 0.921 |
| 0.15 | 0.721 | 0.807 |
| 0.20 | 0.534 | 0.635 |
| 0.25 | 0.407 | 0.401 |
| 0.31 | 0.312 | 0.187 |
| 0.36 | 0.317 | 0.071 |
| 0.41 | 0.144 | 0 |
| 0.46 | 0.083 | |
| 0.51 | 0.038 | |
| 0.56 | 0.011 | |
| 0.61 | 0 | |

(31) was then used to calculate $\Delta\sigma_0$. Table II presents the experimental values of $\Delta\sigma_0$. The errors are statistical (one standard deviation of the mean), and they incorporate the effect of randomized fluctuations in beam velocity, beam shape, and electron-gun characteristics. Since in the range of angles we have explored the scattering-out contribution, given in the right-hand side of Eq. (30) by $Q(E_0)$, is substantially smaller than the scattering-in contribution, the uncertainty in $Q(E_0)$ can be neglected. This situation would change dramatically if data were taken for smaller angles, where the scattering-out contribution becomes dominant as the detector is set closer and closer to the beam axis.

Also shown in Table II are the values of $z_D$ corresponding to each value of $\Theta$, as well as the effective detector collection solid angles,

$$\Delta\Omega = \int_{\Theta_1}^{\Theta_2} d\theta \sin\theta \int_{\Phi_1}^{\Phi_2} \Upsilon(\theta,\phi) d\phi \ . \tag{32}$$

In principle, comparison with theory can be made at this point by folding the theoretical elastic scattering differential cross section with the apparatus form factor $\Upsilon(\theta,\phi)$, defined in Eq. (23). This could be done by computing the integral on the left-hand side of Eq. (30), using Table I for the beam profiles $\mathcal{F}$ and $\mathcal{G}$ and Eqs. (16) and (17) for the limits of integration, with $\alpha L = 19.91$ cm. The beam boundaries are given by $X_1 = -0.41$ cm, $X_2 = 0.61$ cm, $Z_1 = -0.61$ cm, and $Z_2 = 0.41$ cm.

We can also define an "average elastic differential cross section," $\langle\sigma_0(E_0,\theta)\rangle = \Delta\sigma_0/\Delta\Omega$. In general, $\langle\sigma_0(E_0,\theta)\rangle \neq \sigma_0(E_0,\theta)$, but we can determine whether replacing $\sigma_0(E_0,\theta)$ by $\langle\sigma_0(E_0,\theta)\rangle$ is valid by computing $\Delta\sigma_0$ for a given theoretical cross section using the left-hand side of Eq. (30), computing $\Delta\Omega$ using Eq. (32), and then comparing explicitly $\langle\sigma_0\rangle$ with the assumed $\sigma_0$. This was done using the elastic differential cross section computed by Issa[37] for electrons scattering on sodium at 10 eV.[53] Figure 11 shows the results, and it is clear that for angles lower than 7°, $\langle\sigma_0\rangle$ and $\sigma_0$ are essentially identical. We feel that this result justifies doing the same with our experimental results for $\Delta\sigma_0$, and that the error introduced by the averaging over solid angles is negligible compared to the other sources of error in the experiment. The experimental results for $\langle\sigma_0(E_0,\theta)\rangle$ are also presented in Table II; the errors incorporate the statistical error in $\Delta\sigma_0$ and an upper bound for the error in $\Delta\Omega$, arrived at by repeating the computation after introducing reasonable changes in the beam profiles and integration limits. These average differential cross sections are also plotted in Fig. 12, together with the relative measurements of Srivastava and Vuskovic,[13] with their normalization, and the close-coupling results of Issa.[37] It can be seen that our absolute measurements are in quite good agreement with the results of Srivastava and Vuskovic, thus lending support to their data-normalization procedure. Issa's calculations yield results which are in reasonable agreement with experiment, although somewhat low, particularly at 10°, suggesting that forward scattering is underestimated in his work.

TABLE II. Summary of results for the elastic scattering measurements at 10 eV.

| $\Theta$ (deg) | $z_D$ (cm) | $\Delta\sigma_0$ ($10^{-18}$ cm$^2$) | $\Delta\Omega$ ($10^{-3}$ sr) | $\langle\sigma_0(E_0,\theta)\rangle$ (Å$^2$/sr) |
|---|---|---|---|---|
| 12.1 | 0.45 | 18.55±0.84 | 2.97±0.30 | 62.1±6.9 |
| 14.5 | 0.64 | 9.27±0.86 | 2.43±0.24 | 38.1±5.2 |
| 17.0 | 0.88 | 7.67±0.34 | 2.06±0.21 | 37.2±4.1 |
| 19.4 | 1.13 | 7.43±0.23 | 1.81±0.18 | 41.0±4.3 |
| 21.8 | 1.42 | 3.04±0.21 | 1.61±0.16 | 18.9±2.3 |

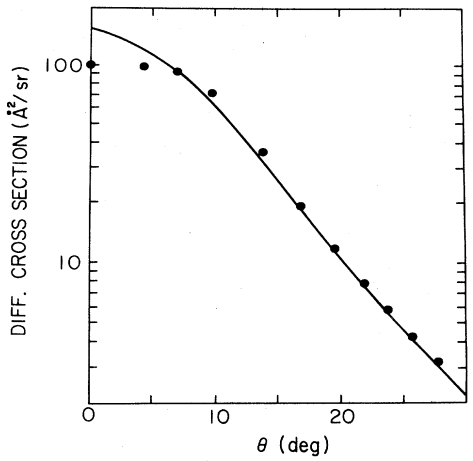


FIG. 11. ($e^-$,Na) elastic differential cross sections vs electron scattering angle at 10 eV. Solid line, two-state close-coupling calculation (Issa, Ref. 37); dots, average differential cross section $\langle\sigma_0\rangle = \Delta\sigma_0/\Delta\Omega$, calculated using the above differential cross section.

## V. SMALL-ANGLE INELASTIC SCATTERING

Figure 13 shows a family of detector signal versus detector position curves obtained by chopping the electron beam at 4 Hz and using phase-sensitive detection on the

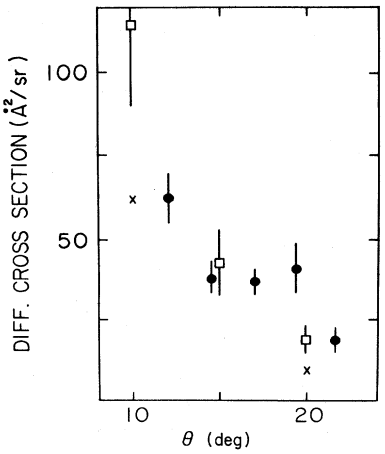


FIG. 12. ($e^-$,Na) elastic differential cross sections vs electron scattering angle at 10 eV. Dots, this work; squares, Srivastava and Vuskovic (Ref. 13); crosses, two-state close-coupling calculations (Issa, Ref. 37). Error bars denote one standard deviation of the mean.

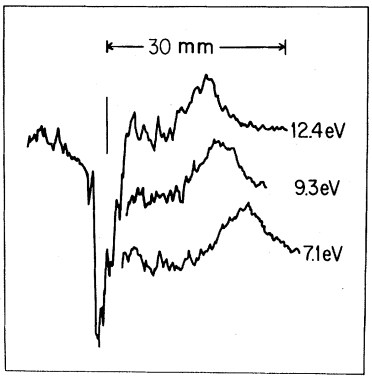


FIG. 13. Phase-locked 4-Hz detector signal vs detector position, for three different electron energies. Vertical line gives the position of the atomic-beam axis. The large dip about the beam axis is the scattering-out signal; the signals become positive when scattering-in becomes dominant. The prominent peaks are the signature of forward scattering after excitation of the $3^2P$ state. Vertical scale is arbitrary, and the zero-signal level for each of the curves has been offset by a different amount for clarity.

Channeltron output, with the Channeltron operating in the analog mode, as described in Sec. II. The large negative signal at the origin represents mainly scattering-out events; when the signal becomes positive, scattering-in becomes dominant. The prominent peaks correspond to electron forward scattering ($\theta=0°$) after excitation of the $3^2P$ state. That process leads to prominent peaks in the angular distribution of the recoiled atoms for two reasons: first, the impact-excitation cross sections are large and dominantly forward; additionally, the azimuthal form factor favors detection of forward scattering events, as shown in Fig. 9. In the case of elastic collisions, forward scattering yields a null recoil angle, and so it cannot be detected, because the recoiled atoms remain within the atomic beam. For inelastic collisions, there is a finite momentum transfer to the atom even for forward scattering, yielding a finite recoil angle $\psi=\alpha-\beta$, and taking out of the atomic beam those atoms which have scattered an electron in the forward direction after the collision. Atoms which have scattered an electron inelastically into the forward direction will cross the detector plane at

$$Z'=(\alpha-\beta)L=[E^{1/2}-(E-E^*)^{1/2}](2m)^{1/2}L/MV\ . \tag{33}$$

The atomic beam has a finite width. In the absence of atomic velocity and electron energy spreads, the atomic beam peak would be displaced by $Z'$ as given by Eq. (33). The spread in peak position due to the electron energy spread will be given by $\delta Z'/Z'\simeq\delta E/[2E^{1/2}(E-E^*)^{1/2}]$. As $\delta E<0.25$ eV, at $E=6$ eV $\delta Z'/Z'\simeq0.025$, and it will be even smaller for higher energies, so that for $E>6$ eV the finite width of the energy distribution can be neglected when computing Eq. (33). Averaging over the atomic velocity distribution yields

$$Z'_P=\langle Z'\rangle=[E^{1/2}-(E-E^*)^{1/2}]\frac{(2m)^{1/2}L}{M}\left\langle\frac{1}{V}\right\rangle\ , \tag{34}$$

where $Z'_P$ is the displacement of the forward inelastic scattering peak from the atomic beam peak. Thus, Eq. (34) allows us to determine $\langle 1/V\rangle$ in terms of the electron energy and the peak displacement. Furthermore, if we neglect the contributions of the electron energy distribution and the finite angular width of the azimuthal form factor, and attribute the broadening of the forward inelastic scattering peak only to the width of the velocity distribution, we can write $[(\Delta Z'_P)^2-(\Delta Z_P)^2]^{1/2}/Z'_P\simeq\Delta V/V$, where $\Delta Z_P$ is the FWHM of the horizontal beam intensity profile, $\Delta Z'_P$ is the FWHM of the forward inelastic scattering peak, and $\Delta V$ the FWHM of the velocity distribution. In this way we obtained an upper bound of 0.25 for $\Delta V/V$.

When the detector is located under the forward inelastic scattering peak, i.e., near $z'=(\alpha-\beta)L$ in Fig. 10, it will also detect atoms which have scattered electrons elastically by larger angles. Typically, for $E=6$ eV, the corresponding elastic scattering angle is $\theta=36°$, and for $E=25$ eV, it is $\theta=17°$. For such values of $\theta$, the azimuthal form factor is quite small, and so the elastic scattering contribution to the signal will be small too. Since the atomic beam has a finite width, there is a finite atomic velocity spread and the azimuthal form factor has a finite angular width, the detector signal will be due to inelastic scattering events within a certain small-aperture cone, rather than strictly forward scattering.

Both $\sigma_1(E_0,\theta)$ and $\gamma(\theta,V,E_0)$ vary very rapidly with $\theta$ near $\theta=0$. Under these conditions we cannot justify performing the integration over the velocity distribution in Eq. (19) independently of the integration over polar scattering angle, as we did for elastic scattering. This, in turn, makes the results of experiments performed as described in Sec. IV difficult to interpret, since we do not know the exact form of the velocity distribution. On the other hand, the ratio of all the atoms recoiled into the forward inelastic scattering peak to all the atoms in the atomic beam will give the probability of scattering an electron into the cone of small aperture defined by the azimuthal form factor, as discussed above, as this is equivalent to following all possible trajectories taking an atom from the beam into the forward inelastic scattering peak.

The number of atoms being inelastically recoiled into a detector centered at $x'=0$, $z'$, of height $d$ and width $dz'$ is

$$dN=2\pi I_e J_0\frac{(2mE_0)^{1/2}}{M}\frac{d}{dL}\mathscr{V}(V)\,dV\,\mathscr{G}(z_0)\sigma_1(E_0,\theta)\times\gamma(\theta,V,E_0)dz_0\,dz'\ , \tag{35}$$

where

$$\theta=\theta(z',z_0;E_0,V)=\arccos[\alpha/\beta+(z_0-z')/\beta L]\ . \tag{36}$$

In Eq. (35) the integration over beam and detector heights has already been performed. The area under the forward inelastic scattering peak is obtained by integrating over $z_0$, $z'$, and $V$:

$$\mathscr{A}_p = 2\pi I_e \frac{d}{Lh} \frac{M}{(2mE_0)^{1/2}} J_0 \times \int dV\, \mathscr{V}(V) \int_{Z_1}^{Z_2} dz_0\, \mathscr{G}(z_0) \int_{Z_1'}^{Z_2'} \sigma_1(E_0,\theta) \times \gamma(\theta,V,E_0)\, dz' , \tag{37}$$

where $Z_1' = z_0 + (\alpha-\beta)L = z_0 + Z_p'$, corresponding to $\theta=0$ scattering, and $Z_2'$ is the position of the far edge of the forward inelastic scattering peak. The residual velocity dependence of the integral over $z_0$ and $z'$ is restricted now to the velocity dependence of the upper limit for $\theta$. Since $Z_2'$ is chosen to be well beyond the forward inelastic scattering peak, the corresponding value of the azimuthal form factor will be small, thus making the velocity dependence of the integral over $z_0$ and $z'$ weak and smooth enough that the integration over the velocity distribution can be now carried out separately. This assumption was tested by performing numerical integration over several different model velocity distributions. Since $\mathscr{V}(V)$ is normalized to unit area,

$$\mathscr{A}_p = 2\pi I_e \frac{d}{Lh} \frac{M}{(2mE_0)^{1/2}} J_0 \times \int_{Z_1}^{Z_2} dz_0\, \mathscr{G}(z_0) \int_{Z_1'}^{Z_2'} \sigma_1(E_0,\theta)\gamma(\theta,V,E_0)\, dz' . \tag{38}$$

The integral in Eq. (38) is evaluated for $V=\bar{V}$.

The area under the atomic beam profile is given by

$$\mathscr{A}_0 = J_0 d \int dV\, \mathscr{V}(V) \int_{Z_1}^{Z_2} \mathscr{G}(z_0)\, dz = J_0 d \int_{Z_1}^{Z_2} \mathscr{G}(z_0)\, dz_0 \tag{39}$$

so that

$$\frac{\mathscr{A}_p}{\mathscr{A}_0} = \frac{2\pi}{N_0} \frac{MI_e}{hL(2mE_0)^{1/2}} \times \int_{Z_1}^{Z_2} dz_0\, \mathscr{G}(z_0) \int_{Z_1'}^{Z_2'} \sigma_1(E_0,\theta)\gamma(\theta,V,E_0)\, dz' , \tag{40}$$

where

$$N_0 = \int_{Z_1}^{Z_2} \mathscr{G}(z_0)\, dz_0 . \tag{41}$$

The cross section for recoiling an atom into the forward scattering peak is

$$\Delta\sigma_1 = \frac{2\pi}{N_0 L} \int_{Z_1}^{Z_2} dz_0\, \mathscr{G}(z_0) \int_{Z_1'}^{Z_2'} \sigma_1(E_0,\theta)\gamma(\theta,V,E_0)\, dz' \tag{42}$$

and then the equation relating $\Delta\sigma_1$ to the observables in the experiment is

$$\Delta\sigma_1 = \frac{(2mE_0)^{1/2}h}{MI_e} \frac{\mathscr{A}_p}{\mathscr{A}_0} . \tag{43}$$

Under these conditions absolute measurement of $\Delta\sigma_1$ is accomplished if $\mathscr{A}_p$ and $\mathscr{A}_0$ are measured at constant detector efficiency and $I_e$ is determined absolutely.

We have measured the ratio $\mathscr{A}_p/\mathscr{A}_0$ at electron energies ranging from 6 to 25 eV. Data have been obtained by chopping the electron gun at 4 Hz and performing phase-sensitive detection of the Channeltron output, the Channeltron being operated in the analog mode. With the detector at a given position, the lock-in amplifier output was sampled repeatedly by the computer ADC, and the measurements were then averaged. This was repeated with the detector set at a large enough number of points across the forward inelastic scattering peak to allow smooth joining of the results. Figure 14 shows a typical set of measurements at a given electron energy. The points to the left and right of the peak are joined smoothly to allow an approximate substraction of the elastic and large-angle inelastic contribution. Many such runs were performed at each of the electron energies that we have investigated. $\bar{V}$ was obtained from the position of the peak, $Z_p' = (\alpha-\beta)L$; the values of $\bar{V}$ obtained in this way through the experiment were very consistent.

The area under the forward inelastic scattering peak, $\mathscr{A}_p$, was measured using a planimeter. $Z_2'$ was also determined from each individual plot, and it was also quite consistent for different runs at the same energy. The area under the beam, $\mathscr{A}_0$, was measured frequently by feeding the Channeltron output into an electrometer with its output connected to the $Y$ input of an $X$-$Y$ plotter. The $X$ input was connected to a position transducer on the $z'$ drive of the detector; the area under the peak tracing was then measured using a planimeter. Calibration runs were performed frequently to determine the gain ratio of the lock-in amplifier and electrometer outputs. Using the necessary scale factors, the ratios $\mathscr{A}_p/\mathscr{A}_0$ were then obtained, and $\Delta\sigma_1$ was calculated for each run. The final results are given in Table III; the errors are statistical (one

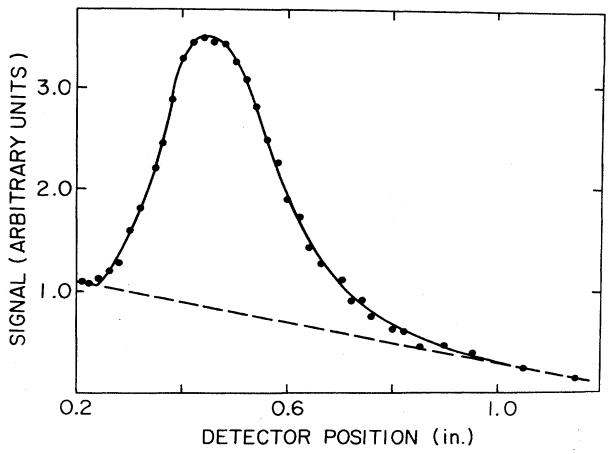


FIG. 14. Computer-integrated phase-locked 4-Hz detector signal vs detector position, at $E_0=22.5$ eV. Dots, experimental data. The smooth-line interpolation was used to determine the area under the forward inelastic scattering peak. Dashed line joining data beyond the edges of the peak allows for rough subtraction of the elastic scattering background. Zero-signal level has been arbitrarily set.

TABLE III. Summary of results for the small-angle impact-excitation measurements.

| $E_0$ (eV) | $Z_p'$ (cm) | $Z_2'$ (cm) | $\Delta\sigma_1$ ($10^{-18}$ cm$^2$) |
|---|---|---|---|
| 6 | 2.39 | 3.43 | 4.06±0.36 |
| 8 | 2.01 | 2.83 | 5.23±0.18 |
| 10 | 1.77 | 2.51 | 6.79±0.19 |
| 12.5 | 1.56 | 2.26 | 8.29±0.13 |
| 15 | 1.41 | 2.14 | 10.8±0.5 |
| 17.5 | 1.30 | 1.97 | 10.8±0.4 |
| 20 | 1.21 | 1.82 | 11.8±0.3 |
| 22.5 | 1.14 | 1.75 | 12.0±0.3 |
| 25 | 1.08 | 1.72 | 12.6±0.6 |

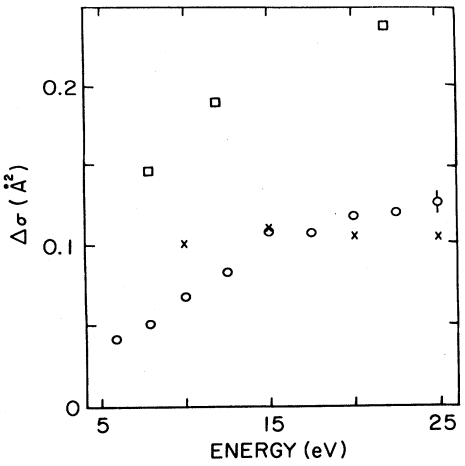


FIG. 15. Effective cross section for sodium atom recoil into the forward inelastic scattering peak vs electron energy. Circles, this experiment; squares, values calculated using the DWPO differential cross sections of Kennedy *et al.* (Ref. 39); crosses, values calculated using the two-state close-coupling differential cross section of Issa (Ref. 37).

standard deviation of the mean), and incorporate the effects of fluctuations in beam velocity, beam shape, and electron-gun characteristics, as in the case of the elastic cross-section measurements. Also given in Table III are the position of the forward inelastic scattering peak at each energy, $Z_p'$, and the position of the far edge of the forward inelastic scattering peak, $Z_2'$. The limits for the integrals over the beam profiles are the same ones given in Sec. IV, and the beam profiles are also the same ones given in Table I. $\alpha L = 5.024 E_0^{1/2}$ cm, and $\beta L = 5.024(E_0 - E^*)^{1/2}$ cm, where $E_0$ and $E^*$ are measured in eV.

The electron polar scattering angle in the integral in Eq. (42) ranges from $\theta = 0$ to fairly large values, of the order of 20°. Since in that interval both $\sigma_1(E_0,\theta)$ and $\gamma(\theta,V,E_0)$ depend very strongly on $\theta$, defining an "average differential cross section" in this case would not be acceptable. Comparison with theory is best accomplished by using Eq. (42) to compute the expected values of $\Delta\sigma_1$ for a given theoretical $\sigma_1(E_0,\theta)$. We have done so far two different calculations: a two-state close-coupling calculation by Issa,[37] and a unitarized distorted-wave–polarized-orbital (DWPO) calculation by Kennedy *et al.*[39] Figure 15 shows the experimental results and the theoretical predictions for both calculations.[53] It can be seen that the DWPO calculation overestimates $\Delta\sigma_1$ by a factor of 3 at the lower energies, and a factor of 2 at the higher energies. Issa's results are in better agreement with our experiment; as the energy increases, his results become progressively lower than ours. This can be interpreted by noting that as the electron energy increases, momentum transfer to the atom for a given scattering angle also increases, effectively reducing the aperture of the cone leading to recoil into the forward inelastic scattering peak. Thus, the trend in Issa's results is most probably due to a insufficiently large small-angle contribution to the scattering cross section.

The DWPO results are generally lower than Issa's for $\theta > 10°$, and become much larger than Issa's for small angles. Comparison with the present experiment suggests then that the DWPO differential cross sections in this energy range are much too sharp in the forward direction. The small-angle differential cross section for impact excitation of the $3^2P$ level must lie somewhere between Issa's results and the DWPO calculation.

## ACKNOWLEDGMENTS

We thank Professor B. H. Bransden for sending us a copy of M. R. Issa's Ph.D. thesis. We also thank Mr. Stanley Lippmann for his help in programming the PDP 11/03 computer controlling these experiments. This research was supported in part by the National Science Foundation, and the atomic-beams apparatus described in this paper was partially funded by a National Science Foundation Capital Equipment Grant.

*Present address: AT&T Bell Laboratories, Holmdel, NJ 07733.

[1]P. J. Visconti, J. A. Slevin, and K. Rubin, Phys. Rev. A **4**, 1310 (1971).
[2]R. E. Collins, B. Bederson, and M. Goldstein, Phys. Rev. A **3**, 1976 (1971).
[3]A. Kasdan, T. M. Miller, and B. Bederson, Phys. Rev. A **8**, 1576 (1973).
[4]B. Jaduszliwer, R. Dang, P. Weiss, and B. Bederson, Phys. Rev. A **21**, 808 (1980).
[5]J. Slevin, P. J. Visconti, and K. Rubin, Phys. Rev. A **5**, 2065 (1971).
[6]W. Gehenn and M. Wilmers, Z. Phys. **244**, 395 (1971).
[7]D. Hils, M. V. McCusker, H. Kleinpoppen, and S. J. Smith, Phys. Rev. Lett. **29**, 398 (1972).
[8]D. Andrick, M. Eyb, and M. Hoffman, J. Phys. B **5**, L15 (1972); M. Eyb and M. Hoffmann, *ibid.* **8**, 1095 (1975).
[9]W. Gehenn and E. Reichert, Z. Phys. **254**, 28 (1972).
[10]W. Williams and S. Trajmar, J. Phys. B **10**, 1955 (1977).
[11]P. J. O. Teubner, S. J. Buckman, and C. J. Noble, J. Phys. B **12**, 3077 (1978).

[12]S. J. Buckman, C. J. Noble, and P. J. O. Teubner, J. Phys. B **12**, 3077 (1978).
[13]S. K. Srivastava and L. Vuskovic, J. Phys. B **13**, 2633 (1980).
[14]R. E. Collins, M. Goldstein, B. Bederson, and K. Rubin, Phys. Rev. Lett. **19**, 1366 (1967).
[15]B. Bederson and T. M. Miller, in *Electron and Photon Interactions with Atoms,* edited by H. Kleinpoppen and M. R. C. McDowell (Plenum, New York, 1976), pp. 191–202.
[16]I. P. Zapesochnyi, E. V. Postoi, and I. S. Aleksakhin, Zh. Eksp. Teor. Fiz. **68**, 1724 (1975) [Sov. Phys.—JETP **41**, 865 (1975)].
[17]E. A. Enemark and A. Gallagher, Phys. Rev. A **6**, 192 (1972).
[18]K. Rubin, B. Bederson, M. Goldstein, and R. E. Collins, Phys. Rev. **182**, 201 (1969).
[19]I. V. Hertel and K. J. Ross, J. Phys. B **2**, 285 (1969).
[20]M. Goldstein, A. Kasdan, and B. Bederson, Phys. Rev. A **5**, 660 (1972).
[21]T. Shuttleworth, W. R. Newell, and A. C. H. Smith, J. Phys. B **10**, 1641 (1977).
[22]S. J. Buckman and P. J. O. Teubner, J. Phys. B **12**, 1741 (1979).
[23]E. M. Karule, in *Atomic Collisions III,* edited by V. Ia. Veldre (Akad. Nauk Latv. S.S.R. Inst. Fiz., Riga, 1965) (Translation TT-66-12939, available through Special Libraries Association Translation Center, John Crear Library, Chicago, pp. 29–48); E. M. Karule and R. K. Peterkop, *ibid.*, pp. 1–27.
[24]D. W. Norcross, J. Phys. B **4**, 1458 (1971).
[25]D. L. Moores and D. W. Norcross, J. Phys. B **5**, 1482 (1972).
[26]E. M. Karule, J. Phys. B **5**, 2051 (1972).
[27]D. L. Moores, J. Phys. B **9**, 1329 (1976).
[28]A. L. Sinfailam and R. K. Nesbet, Phys. Rev. A **7**, 1987 (1973).
[29]A. Temkin and J. C. Lamkin, Phys. Rev. **121**, 788 (1961).
[30]P. G. Burke, in *Atomic Physics I,* edited by B. Bederson, V. W. Cohen, and F. M. Pichanick (Plenum, New York, 1969), p. 265.
[31]P. M. Stone, Phys. Rev. **141**, 137 (1966).
[32]V. K. Lan, J. Phys. B **4**, 658 (1971).
[33]B. H. Brandsen and M. R. C. McDowell, Phys. Rep. **30**, 207 (1977); **46**, 249 (1978).
[34]G. D. Carse, J. Phys. B **5**, 1928 (1972).
[35]L. L. Barnes, N. F. Lane, and C. C. Lin, Phys. Rev **137A**, 308 (1965).
[36]D. F. Korff, S. Chung, and C. C. Lin, Phys. Rev. A **7**, 545 (1970).
[37]M. R. Issa, Ph.D. Thesis, University of Durham, 1977.
[38]H. R. Walters, J. Phys. B **6**, 1003 (1973).
[39]J. V. Kennedy, V. P. Myerscough, and M. R. C. McDowell, J. Phys. B **10**, 3759 (1977).
[40]The quotation marks recognize the fact that many of those are continuum states.
[41]Capable of rotating about vertical (azimuth) and horizontal (altitude) axes.
[42]AerOcoax heater cable, ARi Industries, Inc., Franklin Park, Illinois.
[43]In later experiments this hexapole magnet will also act as an atomic-beam polarizer, providing a beam of alkali-metal atoms in the $m_J=\frac{1}{2}$ manifold of hyperfine states, or, in combination with a second hexapole magnet of similar construction and in rf cavity, as a single hyperfine state selector, providing a beam of alkali-metal atoms in the $F=I+\frac{1}{2}$, $m_F=F$ state.
[44]H. Friedburg and W. Paul, Naturwiss. **38**, 159 (1951).
[45]H. M. Brash, D. M. Campbell, P. S. Farago. A. G. A. Rae, H. C. Siegmann, and J. S. Wylkes, Proc. R. Soc. Edinburgh, Sect. A **68**, 159 (1968/1969, Part II).
[46]COR99 Steel, Corey Steel Co., Chicago, Illinois.
[47]R. E. Collins, B. B. Aubrey, P. N. Eisner, and R. J. Celotta, Rev. Sci. Instrum. **41**, 1403 (1970).
[48]R. E. Collins, Ph.D. Thesis, New York University, 1968.
[49]N. F. Ramsey, *Molecular Beams* (Oxford University, London, 1956), pp. 16–19.
[50]The figure does not show the low intensity ($10^{-4}$ of peak) tails extending several beam widths away from the axis.
[51]B. Bederson and L. J. Kieffer, Rev. Mod. Phys. **43**, 601 (1971).
[52]B. Jaduszliwer, A. Tino, and B. Bederson, Phys. Rev. A **30**, 1269 (1984) (following paper).
[53]Logarithmic interpolation was used to obtain values of differential cross section at intermediate angles.